Soft Matter

PAPER

View Article Online
View Journal



Cite this: DOI: 10.1039/d4sm00729h

# Chirality effects in molecular chainmail†

Alexander R. Klotz, *[a] Caleb J. Anderson[a] and Michael S. Dimitriyev[b]

Received 14th June 2024,
Accepted 15th August 2024

DOI: 10.1039/d4sm00729h

rsc.li/soft-matter-journal

Motivated by the observation of positive Gaussian curvature in kinetoplast DNA networks, we consider the effect of linking chirality in square lattice molecular chainmail networks using Langevin dynamics simulations and constrained gradient optimization. Linking chirality here refers to ordering of over-under versus under-over linkages between a loop and its neighbors. We consider fully alternating linking, maximally non-alternating, and partially non-alternating linking chiralities. We find that in simulations of polymer chainmail networks, the linking chirality dictates the sign of the Gaussian curvature of the final state of the chainmail membranes. Alternating networks have positive Gaussian curvature, similar to what is observed in kinetoplast DNA networks. Maximally non-alternating networks form isotropic membranes with negative Gaussian curvature. Partially non-alternating networks form flat diamond-shaped sheets which undergo a thermal folding transition when sufficiently large, similar to the crumpling transition in tethered membranes. We further investigate this topology-curvature relationship on geometric grounds by considering the tightest possible configurations and the constraints that must be satisfied to achieve them.

## I. Introduction

Many emerging materials are comprised at the microscopic scale of two-dimensional crystalline materials[1] or topologically complex linked-ring molecular architectures such as polycatenanes[2] and Olympic gels.[3] Some materials have combined both features into molecular structures that are both planar and topologically linked.[4,5] There is currently an incomplete understanding about how the underlying topology of the molecular network affects its equilibrium mechanical properties, as well as what role thermal fluctuations play in the stability of planar molecules at finite temperatures. One emerging model system for studying these effects is kinetoplast DNA.

Kinetoplasts are the mitochondrial DNA of trypanosome parasites. Often described as molecular chainmail, they consist of several thousand topologically linked DNA "minicircles" of a few thousand base pairs forming a planar network as well as several dozen "maxicircles" of tens of thousands of base pairs (similar to our own mitochondrial DNA) also linked within the network.[6] Their catenated (linked-ring) molecular structure and planar network topology make them an interesting experimental system for researchers in both the topological chemistry and two-dimensional materials communities.

In one of the initial studies characterizing the material properties of kinetoplasts in free solution, Klotz *et al.* reported positive Gaussian curvature, giving kinetoplasts the appearance of wrinkled hemispheres.[7] There is no known biological reason for this curvature, and it is likely not present in every species. Subsequent work attempted to explain this curvature on physical grounds. Simulations by Polson, Garcia, and Klotz[8] showed that networks of rigid linked rings, when thermalized, will replicate the curvature seen in *Crithidia fasciculata* kinetoplasts. In a detailed simulated-supported atomic force microscopy investigation of kinetoplast DNA, He *et al.*[9] argued that the incommensurability between the area of the kinetoplast sheet and its circumference, which is lined by a dense fiber of excess DNA linkages, creates a tension that is resolved by curving the membrane.

Based on gel electrophoresis experiments,[10] it was concluded that the network structure of *Crithidia* kinetoplasts is that of a honeycomb lattice, with the average number of minicircles each minicircle is linked to, termed the valence, most likely being three. Subsequent investigations, including that of He *et al.*,[9] supported the average trivalence but not the honeycomb picture, which cannot capture the observed complexity of minicircle arrangement. More recent work has investigated the role of the edge loop in determining kinetoplasts topology,[11] as well as that of the maxicircles that are typically neglected.[12] The dependence of the equilibrium structure of a molecular chainmail network on its lattice topology has not been fully explored. Preliminary work by Thomas O'Connor showed that different medieval chainmail designs folded differently at low temperatures,[13] while the simulations by Polson, Garcia and Klotz showed slight differences in the

[a] Department of Physics and Astronomy, California State University, Long Beach, USA. E-mail: alex.klotz@csulb.edu
[b] Department of Materials Science and Engineering, Texas A&M University, USA

† Electronic supplementary information (ESI) available. See DOI: https://doi.org/10.1039/d4sm00729h

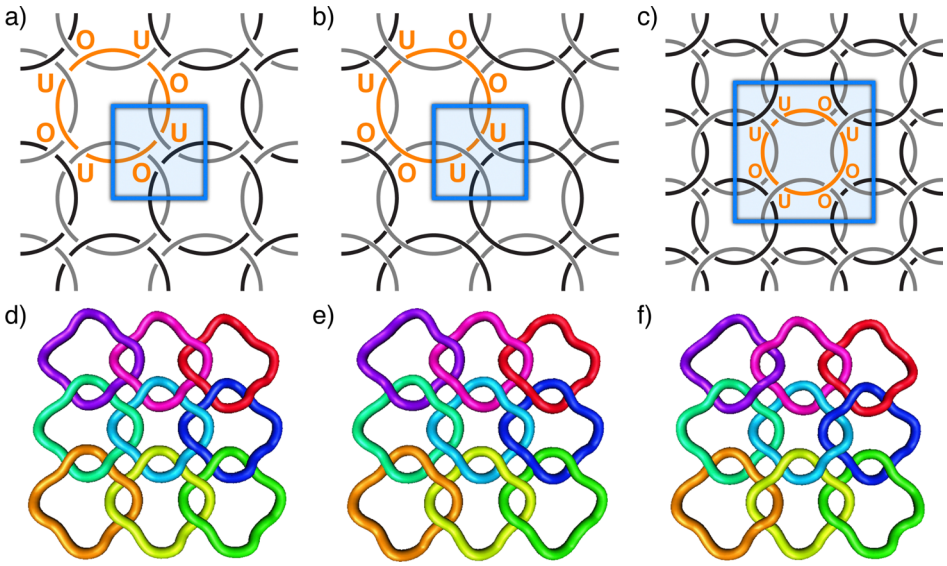


Fig. 1 (a)–(c) Chainmail network topologies shown with unit cells highlighted in blue. Highlighed orange rings have labeled over ('O') and under ('U') crossings. (a) Alternating chirality shows pattern of alternating over-under crossings as a loop is traversed. (b) Non-alternating chirality has pairs of over-crossings next to pairs of under-crossings. (c) Semi-alternating consists of a mix of paired crossings and alternation. Unit cells for (a) and (b) each contain the mass of a single ring; unit cell of (c) contains the mass of four rings. (d)–(f) Initial configurations of 3 × 3 networks of each chainlink network.

concavity of hexagonal and square networks with non-uniform valence.[8] The most detailed simulations by He *et al.*[9] used trivalent honeycomb networks, and highlighted the role of link chirality as well as network topology.

When two solitary rings – curves that form closed loops in three-dimensional space – share a topological Hopf link, a given projection may show that as the path of a single loop is traversed, the link is composed of an under crossing followed by an over crossing, or an over crossing followed by an under crossing. In this case, either loop may be rotated about the plane of projection to change the over-under crossing order to an under-over crossing order. Similarly, a linear chain of Hopf links can interconvert pairs of crossings via rotations of the constituent loops. However, more general linked structures, such as closed necklace-like linked chains or the doubly-periodic chainmail networks shown in Fig. 1, do not admit such flexibility – conversion of under-over to over-under may be achieved via an additional twist of a given loop, rather than a rigid rotation, which adds additional crossings to the projection. Consequently, there are non-equivalent choices of how a given ring passes over and under its neighbors, as encoded by the order of under ('U') and over ('O') crossings, called the "chirality" of the link. We note that the term chirality here does not have the same meaning as is used in knot theory and stereochemistry. For example, the links in Fig. 1(a), with an "alternating chirality," and the links in Fig. 1(b), with "non-alternating chirality," are not mirror images of each other.

The effect of link chirality in polycatenanes and molecular chainmail was explored by Luca Tubiana and collaborators in two studies. The first examined twisted circular polycatenanes,[14] finding that a closed, untwisted, fully non-alternating chain-link will be structurally relaxed at equilibrium, but adding twists before closing the chain link will introduce a torsional constraint to the system that must be alleviated. They formulated a relationship between the number of twists and the apparent writhe of the polycatenane that was analogous to the Fuller–White–Calugareanu relation that applies to supercoiled DNA.[15] In a second study, the simulations used by He *et al.* to explore the effect of tension due to the kinetoplast edge loop,[9] randomized the chirality of each loop such that effects of chirality were averaged out. During the writing of this manuscript, we became aware of parallel work by Luengo-Márquez *et al.*[16] examining the equilibrium properties of block-copolymer chainmail networks with two different link chiralities. The networks simulated by Polson, Garcia, and Klotz[8] used "Japanese-style" networks in which tetravalent or hexavelent rings on a lattice were connected by divalent linkers, eliminating issues with link chirality.

Here, we consider the effect of molecular chirality in square lattices of topologically linked loops. Although the honeycomb lattice is typically used to describe kinetoplast DNA, we choose a square lattice, as the bipartite structure ensures a consistent choice of linking chirality, *i.e.* without the "geometric frustration" characteristic of non-bipartite lattices. Additionally, the 4-valent connectivity yields a bigger difference between the fully alternating and fully non-alternating cases. The three square lattice chiralities that we study can be seen in Fig. 1. Each linked ring contributes a separate over-under (OU) or under-over (UO) pair; since each loop is 4-valent, each loop can be labeled by a sequence of four OU and UO pairs. The fully alternating configuration is given by UOUOUOUO; the fully non-alternating is UUOOUUOO; the semi-alternating is UUOUOOUO. The semi-alternating pattern is known in the armoring community as the European 4-in-1 weave.‡ The unit cells of these networks

‡ Historical armor styles mentioned in this paper are based on the conventions of online communities. We have not examined the historical accuracy of their names.

 

(highlighted blue in Fig. 1) are not centered on the individual loops, but rather the junctions of four loops, with the exception of the semi-alternating network, which is centered on a ring. In Alexander-Briggs and Thistlethwait notation, the unit cells of each network are $8_1^4$/L8a21, $8_3^4$/L8n8, and $8_2^4$/L8n7. As U's and O's only exist in UO and OU pairs, one can consider each pair as labeled with a collective label, *e.g.* an up or down "spin." These chainmail networks then resemble ordered spin arrangements, with the fully alternating case being "ferromagnetic" and the fully non-alternating case being "antiferromagnetic." This suggests a possible mapping of the equilibrium conformations of molecular chainmail to Ising model-patterned elastic sheets, such as those in Plummer *et al.*[17]

In this work, we explore the configurations of molecular chainmail given these chiral topological constraints. We use two complementary numerical methods and a simplified exactly-solvable model. The first numerical method is Langevin dynamics (LD), used to model the equilibrium behavior of polymer chains. We explore the equilibrium configurations of chainmail networks parameterized to the properties of DNA in low ionic strength solvents, comparable to about 13 mM, the second-lowest ionic strength explored in fluorescence experiments with kinetoplast DNA.[18] The equilibrium configuration of a polymer depends on a balance of entropy, excluded volume, and bending rigidity. To reduce the degrees of freedom more directly investigate the relationship between topology and geometry, the second method uses constrained gradient optimization (CGO) to find the tightest possible configuration of chainmail networks, which might arise in synthetic chemical networks.[5] This algorithm is typically used to find the tightest configurations of knots and links, and here is used to identify the minimal geometric factors that lead to the observed membrane behavior. Finally, we develop a simple model of the preferred homogeneous embedding of these networks, illustrating the emergence of intrinsic curvature and the necessity of loop deformation due to an apparent geometric incompatibility between certain periodic linkages and constraints imposed by Euclidean space.

# II. Methods

## A. Initialization

We initialize our loops (a term we use interchangeably with links to refer to the individual components of the networks) as 16-gons. These 16-gons are centered on square lattice sites, and can be thought of as inhabiting tiling squares; initial configurations are shown for the three network chiralities in Fig. 1(d)–(f). Eight vertices of each 16-gon lie in the $xy$-plane in an octagon, with four sides touching neighboring squares in the lattice. Between each two octagonal vertices on the sides of the square, are points extending into the next square, one in the $+z$ direction and one in the $-z$ direction. The order of the $\pm z$ extension determines whether the linkage is over-under or the reverse. Each 16-gon has four linkage components, the alternating 16-gons have all four going over-under. The $z$-coordinates on opposite sides of the 16-gon are flipped to create the fully non-alternating network. To create the semi-alternating network, the $z$-coordinates are flipped on either the upper and right linkage, or the lower and left linkage, and the network is created by a checkerboard tiling of those two cases.

We use spline interpolation to refine the mesh for each loop, increasing the number of vertices-per-loop to $\sim 24$. Because the algorithms we use typically function better with smooth initial configurations, we import the generated configurations into KnotPlot[19] and anneal them by treating each vertex as a charge and each edge as a spring, which ensures evenly-spaced vertices and a safe distance between beads on neighboring links such that they will not cross each other during simulation. After the loops in a medium-sized network have been annealed in KnotPlot, we can extract the coordinates of an interior loop and tile them to create larger networks. Coordinates of these loops and instructions for tiling them are available on the public data repository linked in the data availability statement. For CGO, we also reduce the charge of each vertex and apply a contour-minimizing force in KnotPlot, which allows the minimization to proceed faster.

## B. Langevin dynamics

We simulate molecular chainmail networks with $M$ links using a model used to simulate topologically complex polymers in previous works, and our descriptions may bear similarity to previous descriptions of these methods. In short, each loop in the network is comprised of beads of diameter $\sigma$ (which sets the lengthscale of the system) at position $\mathbf{r}_i(t)$, connected by springs to their two neighbors. A finitely-extensible nonlinear elastic (FENE) spring potential with a maximum extension of $1.5\sigma$ is used. Excluded volume interactions between beads are enforced by a truncated Lennard-Jones repulsive potential that applies when the centers of mass of two beads are closer than $\sigma$. The relatively short range of distances between the excluded volume of the beads and maximum extension of the springs ensures that strands do not cross and the link topology is preserved. Bending rigidity is imposed by a Kratky–Porod potential depending on the cosine of the angle between three successive beads. The strength of this potential sets the persistence length of the polymer. The entire contribution to the energy of a bead is:

$$U_{\text{tot}} = U_{\text{spr}} + U_{\text{ev}} + U_{\text{bend}}. \tag{1}$$

The excluded volume interaction takes the form:

$$U_{\text{ev}} = \begin{cases} 4\varepsilon\left[\left(\frac{\sigma}{r}\right)^{12} - \left(\frac{\sigma}{r}\right)^{6} + \frac{1}{4}\right] & \text{if } r \le 2^{1/6}\sigma \\ 0 & \text{otherwise,} \end{cases} \tag{2}$$

where $\varepsilon$ sets the energy scale of the repulsive interactions. The spring force is parameterized as:

$$U_{\text{spr}} = \begin{cases} -\frac{1}{2}\left(\kappa\frac{\varepsilon}{\sigma^2}\right) R_{\max} \log\left|1 - \left(\frac{r}{R_{\max}}\right)^2\right|, & \text{if } r \le R_{\max} \\ \infty & \text{otherwise,} \end{cases} \tag{3}$$

where $\kappa$ is typically 30 and sets the spring constant in units of $\varepsilon/\sigma^2$ and $R_{max}$ is the maximum separation of the springs, and is $1.5\sigma$ in this work. The bending potential takes the form:

$$U_{bend} = \frac{\ell_p}{\sigma} kT(1 - \cos\theta). \quad (4)$$

The dimensionless ratio of the persistence length $\ell_p$ to the bead diameter is typically $\ell_p/\sigma = 5$ in this work. The time evolution of the $i$th bead is determined by the Langevin equation:

$$m\ddot{\mathbf{r}}_i(t) = -\gamma\dot{\mathbf{r}}_i(t) - \nabla_{\mathbf{r}_i} U_{tot} + \sqrt{2kT\gamma}\boldsymbol{\eta}(t). \quad (5)$$

Here, $\gamma$ is the drag coefficient on a single bead, $kT$ is the thermal energy scale, $\boldsymbol{\eta}$ is a delta-correlated normal random variable, *i.e.* $\langle\eta_i(t)\eta_j(t')\rangle = \delta_{ij}\delta(t - t')$, and an overdot represents a time derivative. The final term provides a random force that emulates Brownian motion in a manner consistent with the fluctuation–dissipation theorem. These equations of motion are solved by LAMMPS,[20] which iterates the system forward in time using the Velocity Verlet algorithm.

The system is non-dimensionalized with $\sigma$, $\gamma$, $m$, $kT$ and $\varepsilon$ taking values of 1, which defines a timescale $\tau = \sigma\sqrt{m/\varepsilon}$. We iterate the simulation with a timestep of $0.01\tau$. We initially perform 500 iterations of the system with a simpler harmonic spring potential to avoid overstretched FENE springs. We then iterate the system for hundreds of thousands to tens of millions of timesteps depending on the system size, typically at least ten times as long as the initial transient deformation of the network from its initial conditions. For each system size, we simulate at least five iterations with different random seeds. To ensure the harmonic equilibration stage did not change the linking topology through strand crossing, we compute the Gauss linking number of neighboring loops in the final configuration and verify that everything is linked appropriately. In practice, this was only an issue for unfavorable initial conditions, which were fixed in KnotPlot.

The equilibrium configuration of a polymer chainmail network depends on four lengthscales: the effective width of the monomers, the persistence length, the contour length of each ring, and the total number of rings. In our simulations, we primarily use a parameterization in which the effective width is set by the diameter of each bead, the persistence length is five beads (representing a monomer anisotropy found in DNA in low-salt solutions), each ring is 24 beads (about 5 persistence lengths), and the number of rings is varied. The simulated polymer rings are comparable to the minicircles of *Trypanosoma brucei*, which are slightly below six persistence lengths in contour. The minicircles in *Crithidia fasciculata* are each about 16 persistence lengths in contour, requiring 80 monomers per ring in this model. While we primarily focus on the system with $M$ rings of 24 beads and a persistence length of $5\sigma$, we will discuss the effect of varying the other lengthscales.

### C. Constrained gradient optimization

We use constrained gradient optimization (GCO) to find the tightest configuration of molecular chainmail networks, that which minimizes the total contour length of all the loops while treating each loop as a tube of unit radius and respecting a no-overlap constraint. The width of a curve is defined as the minimum radius of a circle that is guaranteed to pass through any three points on a curve. The ropelength of a knotted or linked curve is the minimum ratio of the total contour length of the curve to its width. Conventionally, this is normalized such that the thickness of the curve is 0.5 or 1, depending on whether it is treated as a rope with unit diameter or radius. The configuration of a knot or link that minimizes ropelength is known as ideal. No exact value for the ropelength of a nontrivial knot is known, but numeric analyses put the upper bound of the ropelength of the trefoil knot at around 32.74 radii.[21]

To perform constrained gradient optimization (CGO) on chainmail networks, we use an algorithm called Ridgerunner, developed by Jason Cantarella and colleagues. A full description of Ridgerunner can be found in Ashton *et al.*,[21] but in short it approaches the ideal configuration of an initial knot by perturbing its coordinates into many trial knots. At each step, the next perturbation is computed by projecting the gradient of the length function onto a polyhedral cone of perturbations of the current polygon which respect the no-overlap condition. When the projected gradient is a small fraction of the length of the original gradient vector (typically 0.01 or 0.001) the algorithm terminates.

We initialized the three types of square lattice chainmail networks with 9, 16, and 25 loops, with 16 vertices per loop. As a preliminary investigation we also tightened twisted polycatenanes, the system established by Tubiana *et al.*[14] to study chirality effects in linked polymers, discussed in the appendix. We initially performed CGO on the networks using an equilateralization force to maintain a constant distance between the vertices of each loop. When the residual gradient reached 0.1 or the ropelength stopped decreasing, the final configuration was re-run without equilateralization, towards its minimum. Compared to Langevin dynamics and similar methods, CGO is generally slower and limited in system-size as width-testing scales cubically with the number of nodes, and is susceptible to strong local minima. Ridgerunner is not optimized for systems with configurations that have both straight and tightly curved components, such as the links in chainmail networks. Thus, our results should be regarded as approximations to length-minimizing links, within the constraints discussed above.

## III. Results and discussion

### A. Langevin dynamics

For our primary investigation of alternating, fully non-alternating, and semi-alternating chiralities, we arranged loops on square lattices with free boundaries, ranging from $3 \times 3 = 9$ loops up to $15 \times 15 = 225$ loops. We also simulated a more circular network with 137 loops, and performed trial simulations of square Japanese-style chainmail and Borromean chainmail (Appendix). Alternating and fully non-alternating networks were simulated with $M$ = 9, 16, 25, 49, 81, 137, and 225. The behavior of the semi-alternating networks proved more

 

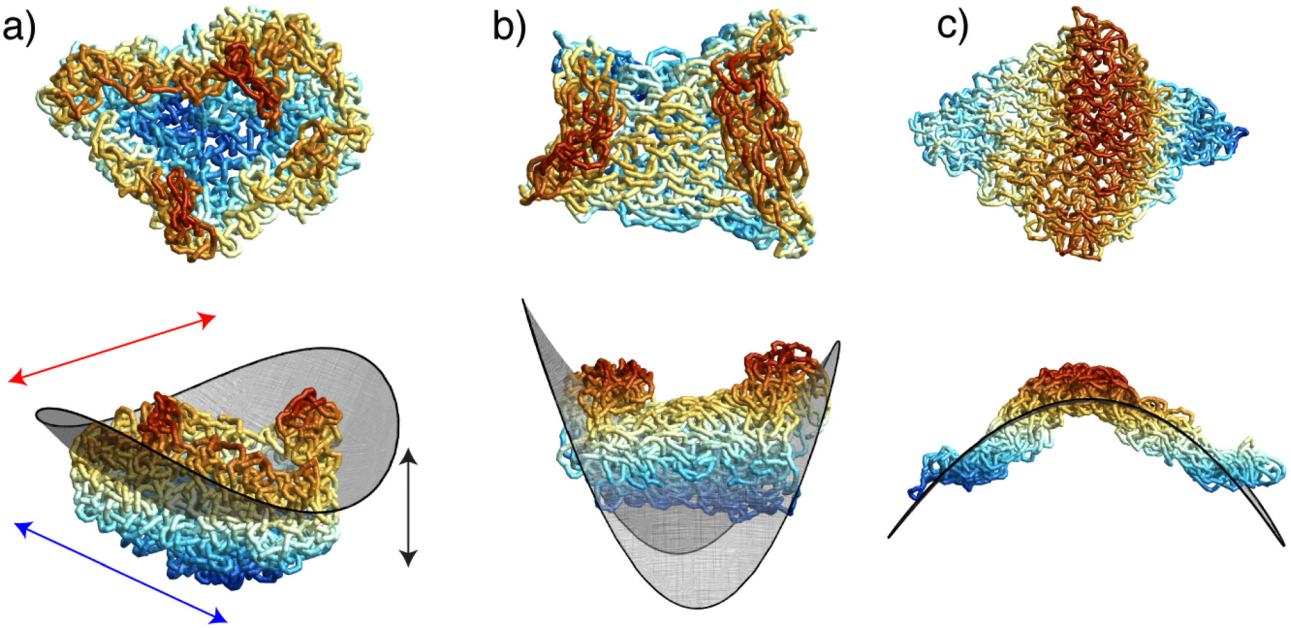


Fig. 2 Representative images of 225-loop molecular chainmail networks simulated with Langevin dynamics for (a) alternating, (b) fully non-alternating, and (c) semi-alternating chiralities. Top row shows a top-down orientation, bottom row shows a side view with an osculating surface. Links are color-coded by their distance along the surface normal direction. The arrows in the bottom-left image represent the principal axes of the gyration tensor.

complex, and thus they were more densely sampled at $M = 9$, 16, 25, 36, 49, 64, 81, 121, 137, 169, 196, and 225.

We begin with qualitative descriptions of the simulated networks, examples of which can be seen in Fig. 2. Videos of three-dimensional rotations of each case may be found in the supplementary data. We observe that alternating networks become bowl-shaped with positive Gaussian curvature, similar to *Crithidia* kinetoplasts. Fully non-alternating networks become saddle-shaped with negative Gaussian curvature. Semi-alternating networks appear flat, although can fold along one axis when sufficiently large, discussed subsequently. In the first two cases, there is little apparent impact of the initially square boundary geometry on sampled equilibrium configurations. Moreover, the edges of the alternating configurations resemble typical edge shapes seen in kinetoplast DNA.[7] In contrast, the semi-alternating lattices elongate along one pair of opposite corners and contracting along another, converging on a diamond configuration with an aspect ratio of about two.

In order to obtain a measure of curvature of each chainmail assembly, we first need to extract a suitable representation of a surface from a given assembly. Here, we generate a Delaunay triangulation of center of mass of each ring, based on the square lattice connectivity. This creates a membrane of plaquettes that meet at nodes, and techniques derived from discrete differential geometry can be used to compute the local Gaussian curvature $K$ and mean curvature $H$ at each node.[22] The Gaussian curvature, here measured in computational units of $\sigma^{-2}$, characterizes the intrinsic geometry of a surface, with positive Gaussian curvature indicating spherical geometries, negative indicating hyperbolic geometries. The node- and time-averaged Gaussian curvature is then a macroscopic representative of intrinsic geometry and is on the order of the inverse square of average radius of gyration of the fluctuating networks. As shown in Fig. 3, the averaged Gaussian curvature is function of network size, with the alternating and fully non-alternating networks exhibiting peak magnitudes at $M = 16$ before approaching zero. The maximum at $M = 16$ can be regarded as a balance between two competing trends: for small $M$, the polymer rings are subject to fewer constraints and are thus able to undergo larger conformational fluctuations, reducing the orientational correlations needed to establish a well-defined curvature; for larger $M$, bending modes of the membranes are more easily excited by thermal fluctuations, leading to inhomogeneous curvature distributions that reduce the average curvature. The semi-alternating networks have a curvature much closer to zero than the others, as expected, but is consistently negative at about $-0.0003\sigma^{-2}$ rather than fluctuating about zero, approaching zero with system size. The notable exception is the circular sheet at $M = 137$, which may be due to the reduction of constraints from a reduced average valence. While the averaged Gaussian curvature of the largest non-alternating network passes zero, Fig. 2(b) reveals that it still samples saddle-shaped configurations. This is confirmed by an alternative surface-construction procedure in which the networks are fit to quadric surfaces, as illustrated in the lower panels of Fig. 2 and discussed in the Appendix.

The parallel work by Luengo-Márquez *et al.*[16] examined two chiralities of the honeycomb lattice and also observed negative Gaussian curvature in systems equivalent to our non-alternating chirality. They examined the local variation of Gaussian curvature across the membrane, and their analysis showed that the time-averaged curvature at each vertex on the surface matched the local curvature of the time-averaged

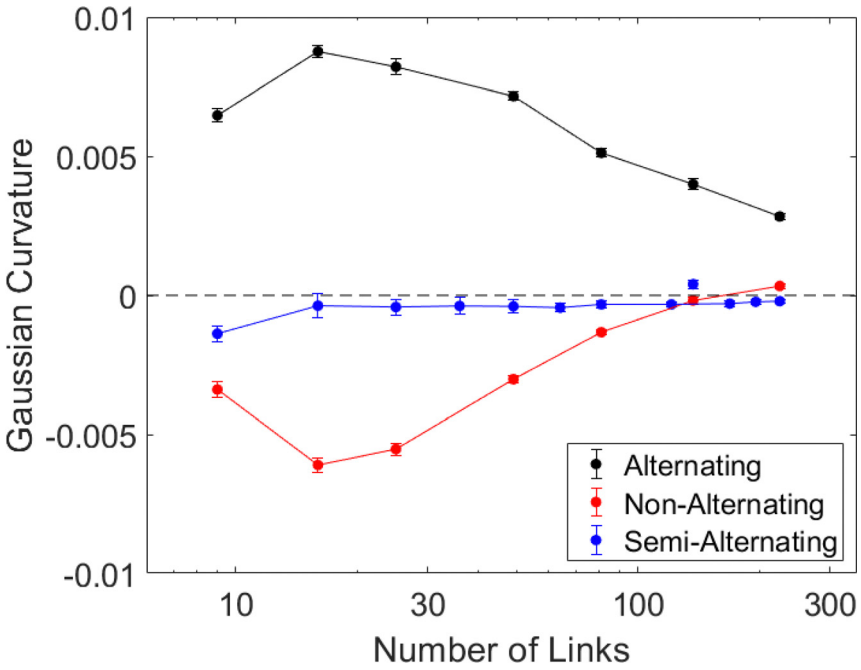


Fig. 3 Gaussian curvature as a function of network size for alternating (black), fully non-alternating (red) and semi-alternating (blue) networks. The datum at $M$ = 137 in each set was taken from a circular rather than square network.

configuration, suggesting that the curvature is stable over long time periods.

To characterize the dimensions of the equilibrated networks, we compute the gyration tensor based on the position of each of $N$ beads relative to the center of mass:

$$G_{ab} = \frac{1}{N}\sum_{i=1}^{N}\left(r_{i,a} - \langle r_a\rangle\right)\left(r_{i,b} - \langle r_b\rangle\right), \qquad (6)$$

where $r_{i,a}$ and $r_{i,b}$ represent the position of the $i$th bead in dimensions $a$ and $b$, and the angle brackets denote the center of mass in that dimension. The eigenvalues of this tensor represent (squared) lengthscales describing the distribution of the network along three perpendicular axes, the eigenvectors corresponding to each eigenvalue. The square roots of these eigenvalues are the principal radii of gyration, and when ordered by size are referred to as the minor, medium, and major axes. For sheet-like networks, there are typically two eigenvectors that point within the plane of the sheet with comparable eigenvalues, and a third pointing transverse to the sheet with an eigenvector that scales with a weaker exponent than those in the plane, sometimes called the roughness exponent. This is known as the "flat" phase,[23] as membranes will extend asymptotically farther in their chemically-defined plane than fluctuate transverse to it. In the flat phase, the in-plane gyration eigenvalues typically grow close to linearly with molecular weight (consistent with area-mass proportionality). Scaling arguments put the roughness exponent near 0.7,[24] which is consistent with simulations.[25–27] The simulation of chainmail networks of rigid circles by Polson *et al.*[8] found in-plane exponents between 0.92 and 1.02 and roughness exponents between 0.73 and 0.84, likely higher than the tethered membrane flat phase due to curvature effects. Fig. 4 shows the scaling of the gyration

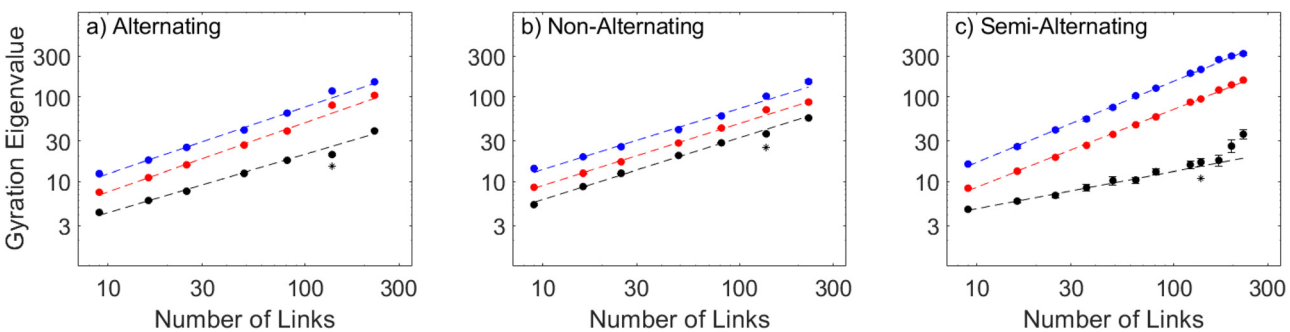


Fig. 4 Squared principal radii of gyration from the eigenvalues of the gyration tensor for alternating (a), full non-alternating (b) and semi-alternating (c) networks as a function of molecular weight, with power-law fits. Each eigenvalue is labelled black, red, and blue in increasing size. The asterisk indicates the 137-ring circular networks that were not used for fits. If not visible, error bars are smaller than points.

 

Table 1 Best-fit scaling exponents of gyration tensor eigenvalues

| Eigenvalue | Alternating | Non-alternating | Semi-alternating |
|---|---|---|---|
| Minor | 0.66 ± 0.02 | 0.74 ± 0.02 | 0.44 ± 0.02 |
| Medium | 0.79 ± 0.02 | 0.73 ± 0.01 | 0.93 ± 0.01 |
| Major | 0.76 ± 0.02 | 0.71 ± 0.03 | 0.95 ± 0.01 |

eigenvalues with system size for the three chiralities. The power-law scaling parameters for each eigenvalue can be found in Table 1. Here we report the dependence on the squared principal radius scaling with molecular weight; other literature may report either the radii or their squares, and either the molecular weight or the side-length, leading to two possible factor-of-two differences in how the exponents are presented (*e.g.* the major eigenvalue in the flat phase is reported in various studies to be close to 0.5, 1, and 2).

The characteristic squared radii of each chirality behave differently with the number of links, and we will discuss them individually. The positively-curved alternating networks have middle and major squared radii that scale with a size exponent between 0.76 and 0.79. This is lower than what is typically found in tethered membrane simulations, including the linked-ring simulation study.[8] The minor exponent of about 0.66 is comparable to some simulations of the flat membrane phase, but should be interpreted as representative of curvature, *e.g.* the depth of the bowl shape adopted by the membrane, rather than roughness. The minor exponent is about 5/6 that of the major exponents, which is comparable to what was observed in the linked ring simulation for rings of finite thickness. The fact that the depth of the bowl grows with a weaker exponent indicates that asymptotically large networks may not appear significantly curved. If, ignoring wrinkles and fluctuations, the membrane took the form of a spherical cap with constant solid angle, all eigenvalues would scale similarly. The smaller transverse scaling is consistent with this angle decreasing with length, or equivalently, the effective radius of the osculating sphere increasing faster than the dimensions of network size. We note that although there is no reason to suspect that kinetoplast DNA has alternating chirality, simulating alternating molecular networks may be a useful method of inducing curvature in future kinetoplast simulation studies.

The negatively-curved, fully non-alternating networks have three principal squared radii that scale with roughly the same exponent, between 0.70 and 0.75. This indicates that they asymptotically adopt an isotropic configuration. Negatively curved saddle-shaped membranes are not common in nature or in synthetic materials, but it is possible to induce negative curvature in origami sheets with specific folding patterns.[28] There have been predictions of nontrivial electronic effects in negatively curved graphene,[29] but this has not been synthesized.

The flat semi-alternating sheets display the most complex behavior. The major and middle squared radii grow with a power close to 1, which is consistent with previous simulations of flat-phase membranes. The roughness exponent takes a value just below one-half, which is smaller than in tethered membrane simulations. We note that the fluctuations of the membrane are anisotropic, taking the form of bends along the long axis of the diamond shape of the membrane, with the short axis remaining stable. This distinctive anisotropy can be rationalized by the underlying symmetry of the network, which possesses a 4-ring unit cell with mirror planes along one diagonal, as opposed to the non-alternating network, which has mirror planes along both diagonals of the unit cell. The correspondingly anisotropic shape fluctuations are analogous to the highly anisotropic elasticity that is seen in knitted fabric, which similarly possess mirror planes along a single direction; the semi-alternating sheets in fact possess a linking motif resembling that of the garter stitch.[30] The lack of fluctuations along one direction likely suppresses the roughness exponent. The finite thickness of the network, due in part to the tendency of each ring to lie with a normal in the plane of the membrane, may suppress roughness further. Notably, the minor eigenvalue of the largest membranes grows faster than the trend set by smaller membranes. This happens when the fluctuations of the long diamond axis become sufficiently large as to cause the membrane to fold over itself, displacing the center of mass from within the loops. This bears similarity to the thermal crumpling transition predicted for tethered membranes, in which the distribution of surface normals lose correlation above a certain thermal lengthscale.[31] It also bears similarity to a backfolding transition observed in nanoconfined DNA that occurs when a molecule exceeds its ''global'' persistence length.[32] A video of a fluctuating semi-alternating network may be found in the supplementary data.

To characterize this folding transition, we note that the diamond-shape networks only fold in the direction of the diamond's long axis, leading to much larger fluctuations in the distance between the two corners separated by the long axis ($D_L$), compared to the two corners separated by the short axis ($D_S$). Typically, the short axis is highly aligned with the medium gyration eigenvector, the eigenvalue of which displays much lower-amplitude fluctuations than the other two, which are anti-correlated. In extreme folding events, the major eigenvector will become aligned with the short axis of the diamond, as can be seen in Fig. 5. These folds are also marked by a displacement of the center of mass of the network away from the geometric center of the middle loop, which greatly increases the minor gyration radius. We can characterize the scale of these fluctuations by measuring the variance in $D_L$ and $D_S$ and plotting their ratio as a function of system size (Fig. 5(b)). This ratio increases with the number of links, but increases much more strongly beyond 100 links. There is evidence of a local maximum at 49 loops that may be indicative of a phase transition.

In contrast to tethered membranes with isotropic interactions that undergo a crumpling transition, the semi-alternating chainmail networks are an anisotropic 2D material, and undergo what can be described as a folding transition rather than a crumpling transition. The thermal lengthscale for crumpling is on the order of $\ell_{th} = \kappa\sqrt{kT/Y}$ where $\kappa$ is the bending modulus and $Y$ is the Young's modulus. Although beyond the scope of this work, future simulations applying uniaxial extension or clamped boundaries may measure these

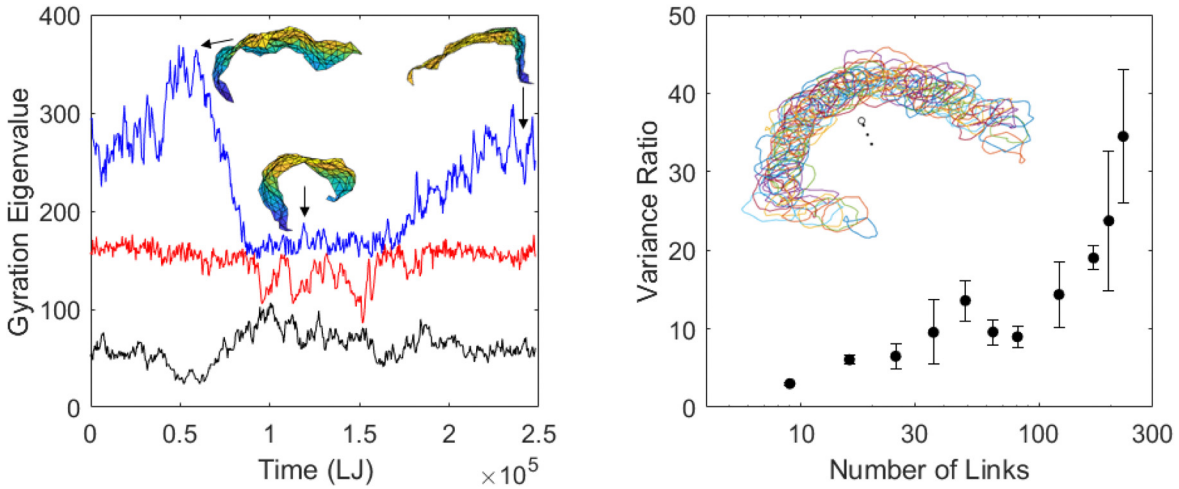


Fig. 5 Left: A partial time series of the three gyration eigenvalues (major, medium, and minor labelled blue, red, and black respectively) of a 225-loop semi-alternating membrane during which a large-amplitude folding event occurs, causing the major axis to align with the width of the diamond-shaped membrane. Delaunay triangulations of the membranes are shown from the side at three stages of this event. Right: Ratio of the variance of the distances between the corners along the long axis of the membrane to the variance of the short axis. Error bars represent standard error over multiple runs. Inset shows a side view of a folded membrane, showing its center of mass as a black circle displaced from the loops, and smaller dots pointing along the minor eigenvector.

moduli to further clarify the lengthscale associated with the folding transition.

There are many possible extensions to this model that can be explored, and as the main focus of this manuscript is chirality we will only comment on them qualitatively. Other lattices besides square can be studied, and we direct readers to the works of Luengo-Marquez *et al.*[16] and He *et al.*[9] for simulations of honeycomb lattices. Rings may be removed from the networks to simulate kinetoplast degradation experiments; we observe that when 10% of the rings are randomly removed the curvature is not affected, but the networks lose their sheetlike properties when 20% are removed. Introducing a small number of random lattice defects with the opposite chirality does not impact the overall curvature, but there likely exists some critical fraction of defects that will. The Lennard-Jones repulsion in our simulations ignores the screened electrostatic repulsion between DNA segments; if the charged repulsion is included the simulations, the same curvature is observed but segments in each ring become significantly stretched. In the two previous kinetoplast simulation studies, the minicircles were rigid or effectively rigid: Polson, Garcia, and Klotz simulated rigid circles,[8] and He *et al.* simulated rings with a contour length half of the persistence length.[9] As mentioned, the minicircles in *T. brucei* kDNA are about 1000 base pairs or six persistence lengths, while in *Crithidia fasciculata* they are about 2500 base pairs or 16 persistence lengths. Alternating networks can pucker when the persistence length is increased, similar to puckering observed by He *et al.*[9] Fully non-alternating networks lose some isotropy and become more taco-shaped. Semi-alternating networks remain diamond-shaped. When the persistence length is kept the same but the loops are increased to 80 beads to mimic *Crithidia* minicircles, we do not see curvature effects as strongly. This is likely due to the reduced excluded volume interactions between the rings, and we expect that sufficiently large networks would revert to the established trends.

### B. Constrained gradient optimization

We annealed towards the ideal configurations of the three square lattice chiralities with 9, 16, and 25 loops. Larger networks were attempted but did not converge on a minimal configuration, even with more vertices per loop. As a preliminary investigation, we annealed polycatenanes with varying degrees of twist to measure the effect of intrinsic twist on ropelength, described in the Appendix.

We begin with a qualitative description of the ideal networks. Examining the tight configurations in Fig. 6, the alternating, non-alternating, and semi-alternating networks display positive, negative, and null Gaussian curvature as in the polymer simulation. The semi-alternating case in particular remains effectively flat with increasing size. Quantitatively, we can measure the total contour length of the network, in addition to the radii of gyration and the Gaussian curvature.

The lower bound on the ropelength of a linked network follows a result from Cantarella *et al.*[33] that each loop in the network that is Hopf linked to $Q$ neighbors cannot be shorter than a curve that is parallel (and one unit separated) to the minimum convex hull around $Q$ unit-radius disks. While the minimum convex hull is a challenging optimization problem when $Q$ is large, each link in square lattice molecular chainmail has either 2, 3, or 4 linked neighbors. The ideal divalent link is a stadium curve of length $4\pi + 4$, the ideal trivalent link is a rounded triangle with length $4\pi + 6$, and the ideal tetravalent link is a rounded square or rhombus with a length of $4\pi + 8$. A square network with $M = L^2$ components will have $(L-2)^2$ tetravalent links in the interior, $4(L-2)$ trivalent links on the

 

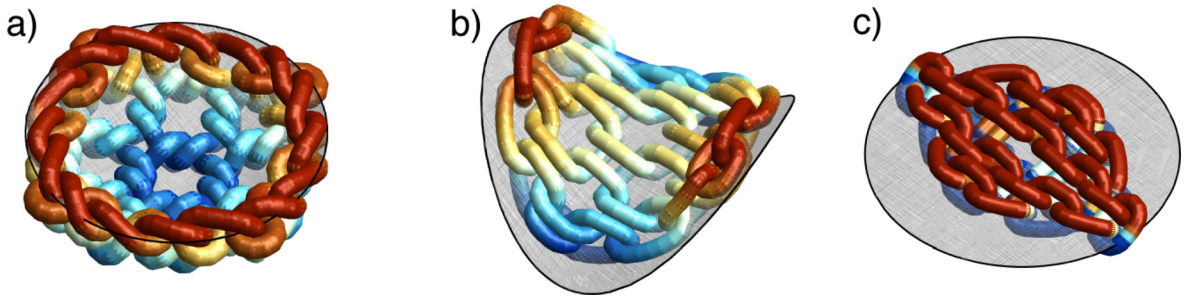


Fig. 6 Renderings of the tightest configurations of (a) alternating, (b) fully non-alternating, and (c) semi-alternating chainmail with 25 links, with osculating surfaces. Links are colored by their position along the surface normal direction.

edges, and 4 divalent links in the corners. For networks of side length $L$ = 3, 4, 5, this gives lower bounds of approximately 161.1, 297.1, and 474.2.

We can compare the total contour length of each network to the lower bound. In all cases, the excess contour increases with the number of links. The alternating network exceeds it by the most, by 31%, 39%, and 47% with 9, 16, and 25 links. The non-alternating exceeds the minimum by 7%, 13%, and 29%, and the semi-alternating is the closest to the ideal configuration, exceeding it by 4%, 6%, and 12%. It may be argued that the larger networks are simply not being annealed as efficiently, but it is likely that the loops on the edge do not need to twist as much to accommodate the topological constraints, and larger networks have a larger proportion of interior loops. The mean and Gaussian curvature of each network can be compared to the expected behavior of surfaces. Here, we expect the ratio of Gaussian curvature to the square of mean curvature to be unitary for surfaces of positive Gaussian curvature, to diverge to negative infinity for surfaces with negative Gaussian curvature, and zero for flat surfaces. Examining the 25-link tightened networks in Fig. 6, we find values of 0.999982, −201.824 and 0.779 respectively. We note that the curvature of a tight configuration does not necessarily dictate the equilibrium conformation of a polymer model of the same network. For example, a Japanese-style square network can be constructed in a plane out of ropelength-minimizing components, but maintains positive Gaussian curvature as a polymer (Fig. 11).

Although the annealed networks approach the lower bound of ropelength to within tens of percent, it is clear from visual inspection that many of the configurations have not reached their true minimum. This is likely due to the fact that Ridgerunner is optimized for tightening sections of densely linked curves, but not for reducing the length of the straight segments of each link. While these results do highlight the role of topological constraints in the chirality-curvature relationship, they remain qualitative.

In addition to the overall properties of the tight networks, we can examine the tightest shape of the links from the interior, edges, and corners of the networks. Examples for each position and chirality are seen in Fig. 7. The out-of-plane deviation of each ring must accommodate its neighbors according to the chirality, with the flat networks remaining the most planar. The divalent corner loops in the alternating case appear to be twisted into a figure-8 shape, which is also observed in the corner loops in the networks simulated using Langevin dynamics. Although kinetoplast minicircles are typically not supercoiled, this indicates how an "open circular" molecule may have a twisted shape due to external topological constraints.

## IV. Link chirality and Gaussian curvature

We now derive a relationship between linking chirality and the Gaussian curvature of a chainmail sheet by considering a

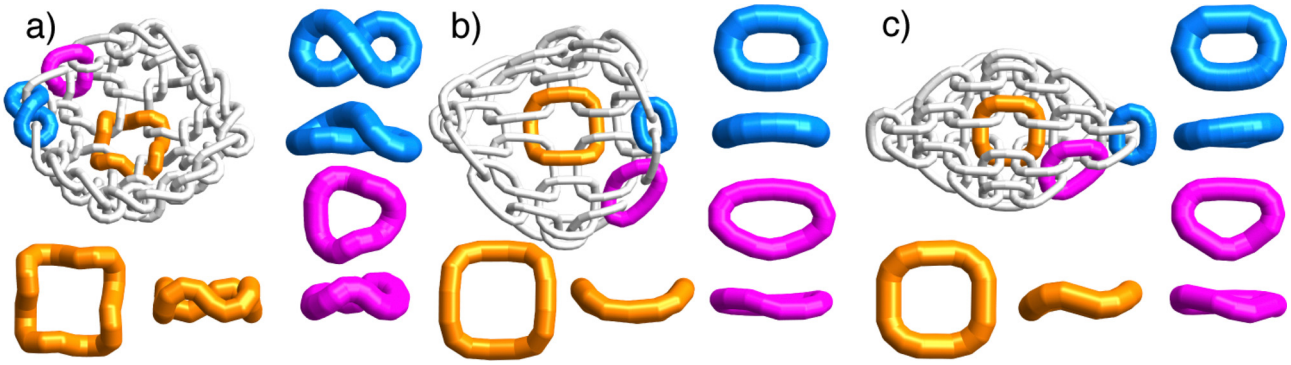


Fig. 7 Individual links in tightened networks from the interior (orange), edge (magenta), and corner (blue) of networks with alternating (a), non-alternating (b), and semi-alternating (c) chiralities.

minimal geometric model of linked rings. In the systems considered so far, the fundamental unit is a closed loop of material whose equilibrium shape deviates from a circular ring of some radius $R$. In the case of ring polymers, the expected circular conformation is the ensemble-averaged configuration of a solitary ring polymer; for tight ropes, the circular ring minimizes ropelength while maximizing the amount of area that the rope can enclose. Deviations from these ideal states can arise from interactions between linked loops: there may be either a reduction in conformational entropy or an increase in ropelength when rings become linked. Since each ring has a finite thickness $t$, two rings that are linked together are required to pierce through the interior of the other ring, so that of the $\approx \pi R^2$ of interior area, each linked ring decreases the amount of "empty area" by $\sim t^2$, constraining the states available to the rings: ropes cannot be tightened to arbitrarily small lengths and ring polymers experience a reduction in conformational entropy. Since this threaded area depends on the orientation of the two linked rings, given by the normal unit vector $\hat{\mathbf{N}}$, *via* a function that increases with $\hat{\mathbf{N}}^1 \cdot \hat{\mathbf{N}}^2$ (here, 1 and 2 index the two linked rings), the optimal configuration is one where the rings are mutually orthogonal. Just as Hopf links between pairs of rings in a linear chain can freely exchange the order of over-under crossings, such linear chains can freely rotate so that neighboring rings have orthogonal orientations. Similarly, as ring networks lack this freedom to exchange the order of crossings, rings cannot remain orthogonal in these networks – we now explore consequences of this linking frustration.

To describe the geometry of a collection of rings, we first define an orthonormal frame $\{\hat{\mathbf{d}}_1, \hat{\mathbf{d}}_2, \hat{\mathbf{N}}\}$ for a given ring, where $\hat{\mathbf{d}}_\mu$ ($\mu = 1, 2$) lie in the plane of the ring. Arranging these rings on a square lattice, we can then index the rings by a pair of integers $(i,j)$. If each ring is assumed to be identical (ignoring boundaries), we can treat the chainmail sheet as a homogeneous surface, where points on the surface correspond to ring centers $\mathbf{r}^{(i,j)}$; the normal vector at each point is $\hat{\mathbf{N}}^{(i,j)}$ and the tangent space at each point is spanned by the vectors $\hat{\mathbf{d}}_\mu^{(i,j)}$. Next we will orient the tangent basis vectors such that $\hat{\mathbf{d}}_1^{(i,j)}$ is parallel to $\mathbf{r}^{(i+1,j)} - \mathbf{r}^{(i,j)}$ and $\hat{\mathbf{d}}_2^{(i,j)}$ is parallel to $\mathbf{r}^{(i,j+1)} - \mathbf{r}^{(i,j)}$, both in the limit of $R \to 0$. The orientations of neighboring rings can be related by a pair of Euler angles – a bending angle $\theta_\mu$ and a twisting angle $\psi_\mu$ – that detail the rotation of a ring's normal vector into its tangent plane. The rotation matrices $\mathcal{R}_\mu\left(\theta_\mu, \psi_\mu\right)$ (provided in the Appendix) that describe this rotation operation then define a discrete affine connection. Importantly, rotations that fix the normal vector do not play a role. Next, consider a situation in which $t \ll R$ and linked rings are in contact at their boundaries. Then neighboring ring centers can be related *via*

$$\begin{aligned} \mathbf{r}^{(i+1,j)} - \mathbf{r}^{(i,j)} &\approx \frac{R}{2}\left(\hat{\mathbf{d}}_1^{(i,j)} + \hat{\mathbf{d}}_1^{(i+1,j)}\right) \\ \mathbf{r}^{(i,j+1)} - \mathbf{r}^{(i,j)} &\approx \frac{R}{2}\left(\hat{\mathbf{d}}_2^{(i,j)} + \hat{\mathbf{d}}_2^{(i,j+1)}\right) \end{aligned} \tag{7}$$

and the full shape of the chainmail can be constructed given a set of bending and twisting angles.

Given the affine connection and eqn (7), we can assess the degree to which the chainmail sheet can be approximated by a smooth, homogeneous membrane in Euclidean space. We do this by examining a closed circuit along the lattice – a path $\mathbf{r}^{(i,j)} \mapsto \mathbf{r}^{(i+1,j)} \mapsto \mathbf{r}^{(i+1,j+1)} \mapsto \mathbf{r}^{(i,j+1)} \mapsto \tilde{\mathbf{r}}^{(i,j)}$ – and determining the magnitude of the displacement vector $\mathbf{u}$ required to join the ring center $\mathbf{r}^{(i,j)}$ (the origin of the circuit) to the ring center $\tilde{\mathbf{r}}^{(i,j)}$ (the end-point of the circuit), as depicted in Fig. 8(b). The lattice circuits for non-alternating and alternating chainmail are shown in Fig. 8(c) and (d). Lattice symmetry dictates

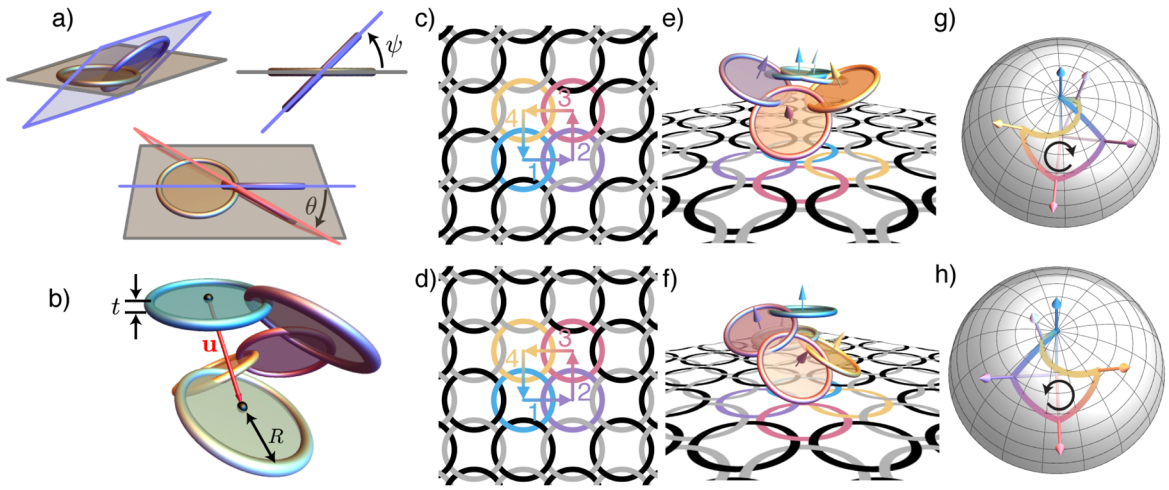


Fig. 8 (a) Depiction of the twist angle $\psi$ and bend angle $\theta$ for two linked rings. (b) A non-closed configuration of a chain of linkages, where $R$ is the ring radius, $t$ is the ring thickness, and $\mathbf{u}$ is the vector joining the end of the chain to the beginning. Closed circuits are shown on the diagrams representing the (c) non-alternating chainmail and (d) alternating chainmail, where the order 1–4 shows the counterclockwise ordering of the path. (e) and (f) Show these linkage circuits in Euclidean space, where $\psi = \pi/10$ and $\theta$ minimizes $|\mathbf{u}|^2$, for non-alternating and alternating chainmail, respectively; arrows represent the orientations of these rings. (g) and (h) Show the Gauss maps of these circuits, with clockwise path indicating a negative curvature and counterclockwise path indicating a positive curvature.

 

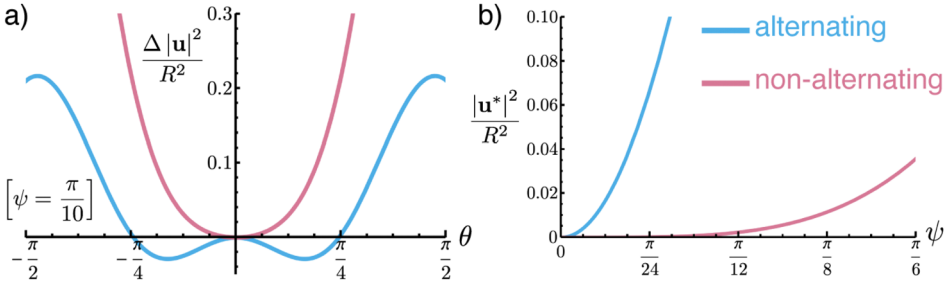


Fig. 9 (a) Compares the degree of nonclosure, expressed as $\Delta|\mathbf{u}|^2 \equiv (|\mathbf{u}(\theta,\psi)|^2 - |\mathbf{u}(0,\psi)|^2)/R^2$, as a function of bend angle $\theta$ for twist angle $\psi = \pi/10$. (b) Compares the minimum value of the non-closure $|\mathbf{u}^*|^2/R^2 \equiv |\mathbf{u}(\theta^*(\psi),\psi)|^2/R^2$ as a function of twist angle $\psi$.

relationships amongst the bending angles $\theta_\mu$ and twisting angles $\psi_\mu$, such that for the non-alternating lattice, $\theta_2 = -\theta_1 \equiv -\theta$ and $\psi_2 = -\psi_1 \equiv -\psi$, and for the alternating lattice, $\theta_2 = \theta_1 \equiv \theta$ and $\psi_2 = \psi_1 \equiv \psi$. Since vanishing values of the twist angle $\psi$ result in rings whose boundaries pass through each other, thus requiring rings to deviate from their preferred circular shape, we fix $\psi$ to be non-zero and then consider values of $\theta$ that minimize $|\mathbf{u}|^2$. The case of $\psi = \pi/10$ is shown in Fig. 8(e) and (f) for non-alternating ($\theta = 0$) and alternating ($\theta \approx 0.513$) chainmail, respectively, revealing that these linkages do not generally close in Euclidean space. At fixed $\psi$, the magnitude of non-closure is shown as a function of bending angle $\theta$ in Fig. 9(a). While non-alternating sheets minimize their non-closure by twisting without bend ($\theta = 0$), alternating sheets adopt one of two non-zero bend angles $\pm\theta^*(\psi)$. In a small-angle approximation, we find for alternating sheets that the degree of non-closure is given by

$$\frac{\Delta|\mathbf{u}(\theta,\psi)|^2}{R^2} \equiv \frac{|\mathbf{u}(\theta,\psi)|^2 - |\mathbf{u}(0,\psi)|^2}{R^2} \approx -\frac{5}{2}\psi^2\theta^2 + \frac{1}{2}\theta^4, \qquad (8)$$

so that the optimal bending angle is $\theta^*(\psi) \approx \pm\sqrt{\frac{5}{2}}\psi$.

The failure of circuits of rings to close suggests that each circuit in the lattice may be treated as enclosing a dislocation core and the closure of these circuits requires an elastic deformation from the preferred state, the cost of which scales with $|\mathbf{u}|^2$.[34,35] Since the amount of dislocation grows with the number of rings enclosed by the lattice circuit, the elastic cost grows super-linearly with respect to network size, requiring increasingly large deformations at the boundary of the sheets, thus limiting their maximum sizes,[36,37] and resulting in large differences in the shapes of bulk and boundary loops, as illustrated in Fig. 7. As shown in Fig. 9(b), the cost of elastic deformation is smaller for non-alternating sheets, increasing as $|\mathbf{u}^*(\psi)|^2/R^2 \approx \frac{1}{2}\psi^4$, whereas for alternating sheets, $|\mathbf{u}^*(\psi)|^2/R^2 \approx 4\psi^2 - \frac{95}{24}\psi^4$. Consequently, alternating sheets are under higher residual stress when forced to maintain closed links in Euclidean space.

Finally, we can calculate the expected curvatures of these sheets by studying the transport of the ring frame around a lattice circuit. The curvature is related to the net rotation of the frame around a closed circuit, which is given by the commutator of $\mathcal{R}_1$ and $\mathcal{R}_2$, namely $\mathcal{R}_{\text{circ.}} \equiv \mathcal{R}_2^{-1}\mathcal{R}_1^{-1}\mathcal{R}_2\mathcal{R}_1$. Taking the small-angle approximation, we find that

$$(\mathcal{R}_{\text{circ.}})_{ij} \approx \delta_{ij} - (\theta_1\theta_2 + \psi_1\psi_2)\varepsilon_{ij3}, \qquad (9)$$

where $\varepsilon_{ijk}$ is the Levi-Civita symbol. We find that to leading order in the bending and twisting angles, the frame undergoes an in-plane rotation when transported around a circuit, indicating that the Gaussian curvature $K$ is given by

$$K_{\text{non-alt.}} \approx -\frac{\psi^2}{R^2} \qquad (10)$$

for non-alternating chainmail and

$$K_{\text{alt.}} \approx \frac{7\psi^2}{2R^2} \qquad (11)$$

for alternating chainmail. Therefore, we confirm that non-alternating chainmail is characterized by negative Gaussian curvature (*i.e.* is hyperbolic) and alternating chainmail is characterized by positive Gaussian curvature (*i.e.* is spherical), as seen in the results of both simulations. The identification of the alternating chainmail as spherical allows us to interpret the two preferred bending angles as corresponding to the two choices sign for the mean curvature $H \approx \pm\sqrt{5/2}\psi/R$. Beyond the small-angle approximation, we additionally consider transport of the normal vector $\hat{\mathbf{N}}$ around the lattice circuit. The unit vectors are mapped to the unit two-sphere *via* the Gauss map, and the individual ring normals form the corners of the paths shown in Fig. 8(g) and (h) for non-alternating and alternating chainmail, where the segments of the path are found using linear interpolation. The solid angle formed by the paths on the unit two-sphere is proportional to the integrated Gaussian curvature of the surface patch that they represent, and the orientation of the path is controlled by the sign of the Gaussian curvature, providing a secondary confirmation that the two chainmail sheets have different curvatures.[38] Notably, these paths do not close, indicating a net rotation of the normal that is not found in the small angle approximation. This suggests a net twist or torsion of the frame as it is transported around the circuit. Since surfaces are not allowed to have torsion, this is another source of stress that must be accounted for by ring deformation in order for the sheet to be embedded in Euclidean space.

# V. Conclusion

The most significant result of this work is a set of simulation data and a complementary model showing the connection between the chirality of links in molecular chainmail and the Gaussian curvature of the surface. We have demonstrated this both for a DNA-parameterized polymer model, and for geometrically tight ideal configurations. We have observed that networks with semi-alternating chirality that are flat at small molecular weights will undergo a transition to folded configurations above a certain size, analogous to the crumpling transitions predicted for tethered membranes.

Analogous systems are subject to theorems relating curvature to chirality in some way. The Fuller–White–Calugareanu theorem relates the topology and geometry of a twisted ribbon (or a DNA double-helix), constraining the sum of twist and writhe of the ribbon to the linking number of its two edges (or helices). Likewise, the Gauss–Bonnet theorem relates the Gaussian curvature of a surface to its donut-hole genus. An analogous theorem may be developed to relate the chirality of a linked surface to its Gaussian curvature. Drawing on the similarity between the polymer and tight networks in Fig. 2 and 6, a constraint may be established (for example) between the Mobius energy of the links and the Helfrich energy of the surface. As a first step towards such a relation, we have developed an understanding of the topology-curvature relation through a model system of linked rigid rings. This purely kinematic construction, which shares similarities with geometric relations for periodic origami,[39] defines a discrete affine connection based on the constraints introduced by the configuration of Hopf links between pairs of rings. Intrinsic curvature is then derived from the holonomy of this discrete connection. Since this construction is purely based on local rules, without *a priori* postulating a specific manifold structure, we find predictions for rings that preferentially lie in defect-ridden lattices, suggesting that a geometry-curvature relationship for periodically-linked rings in the spirit of Fuller–White–Calugareanu may resemble the relationships between topological defects and curvature of flexible crystalline membranes.[40] Notably, our model establishes the emergence of curvature as a consequence of ''linking frustration,'' originating from the topological constraints on linking in each ring network that is not present for linear chains; it may be regarded as a many-body effect. Moreover, the observed relationships between link symmetry and membrane shape draws parallels with similar relationships between stitch topology and fabric shape and mechanics in the context of knitted fabric,[30] which we leave for future explorations. Finally, we emphasize that the networks studied here are quite different in structure from kinetoplast membranes, which are unlikely to have a uniform chirality and whose curvature is likely boundary-controlled. Nevertheless, we find preliminary evidence that the predicted sign of Gaussian curvature survives modest changes in coordination and removal of rings, suggesting that the averaged membrane curvature depends on a more general distribution of network chiralities; such a relationship between linking statistics and intrinsic geometry remains unexplored. We hope that this work allows the discovery of a more complete understanding of the topology-curvature relation for surfaces, and guides the rational design of future planar materials with topologically complex chemistry.

# Data availability

Raw data used for plots, initial configurations, as well as LAMMPS and Ridgerunner simulation outputs, can be found at the Harvard Dataverse at **https://doi.org/10.7910/DVN/ADEG8U**.

# Conflicts of interest

There are no conflicts to declare.

# Appendices

### Tight twisted polycatenanes and bonus networks

Here we discuss the results of constrained gradient optimization of twisted polycatenanes using Ridgerunner. For an introduction to twisted polycatenanes we direct the reader to Tubiana *et al.*[14] We initialized polycatenanes as circular networks of 22-gons, each with two possible link chiralities. The polycatenanes had an even number of links. If all links have the same chirality, the network is fully non-alternating and untwisted. If a link had the opposite chirality of its two neighbors, it gives the network alternating crossings and excess twist. A network is said to be maximally twisted if half the links contribute to twisting the network. When the polycatenane is fully non-alternating and untwisted, each link may be minimized to a stadium curve with ropelength $4\pi + 4$,[33] and the network takes on a familiar chain-link configuration with a ropelength of $M(4\pi + 4)$. The simplest links that admit this pattern are the 4-component $8_3^4$, $8_2^4$, and $8_1^4$ with zero, one, and two twists.

We measured the ropelength of twisted polycatenanes with $M$ from 6 to 18 loops, varying the twist from zero to $M/2$. Untwisted polycatenanes formed circular chain-link configurations as expected, and as the twist was increased, each component in the network became twisted. The final configuration often picked up the symmetry of a regular $M/2$-gon, for example the 8-loop polycatenane forming a square (Fig. 10(a)). The process often involved a buckling in which the normal vector of each loop was forced to rotate 180°. Since the ropelength depends more strongly on the number of loops than their twist, we plot the ratio of the measured ropelength to the untwisted minimum, against the degree of twist $\frac{N_{\mathrm{tw}}}{M/2}$ ranging from 0 to 1. Fig. 10(b) shows this data for polycatenanes with 4, 8, and 16 loops. Although the excess ropelength similarly increases with twist for each sized network, the maximum excess ropelength at maximum twist is largest for the smallest networks. The excess ropelength at maximal twist as a function of the number of loops in the network is plot in Fig. 10(c), where it decreases

 

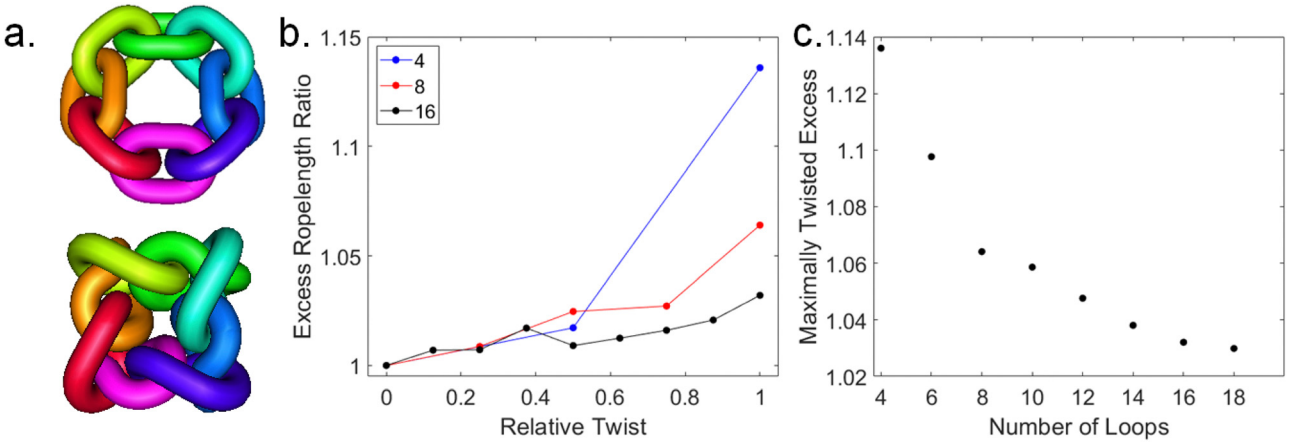


Fig. 10 (a) Ideal configurations of untwisted and maximally twisted 8-loop polycatenanes. (b) Excess ropelength ratio of ideal twisted polycatenanes, as a function of their relative twist as defined in the text. (c) Excess ropelength ratio of maximally twisted polycatenanes as a function of the number of loops.

roughly as $1 + 2/M$. The tightest knot is not necessarily the smallest,[41] and the maximally twisted polycatenanes, despite having a greater ropelength, occupied a smaller volume as defined by their convex hull. This may have implications for the evolution of supercoiling in bacterial DNA

In a square lattice chainmail network, each set of $3 \times 3$ loops maybe treated as an 8-loop polycatenane constrained by a ninth in the middle. We expect alternating networks to have loops that are more deformed from their ideal configuration than the comparable maximally-twisted 8-loop polycatnenaes in Fig. 10(a), acquiring at least 6% excess ropelength. Although direct comparisons between polycatenanes and chainmail networks are difficult, this was a necessary first step towards our current understanding.

Fig. 11 shows the patterns and sample LAMMPS configurations of Japanese 4-in-1 chainmail, studied by Polson *et al.*,[8] and Borromean chainmail, based on a design by Luc Devroye.[42] Japanese chainmail has no chirality effects, and no two links in Borromean chainmail share a direct topological link. We have not done quantitative analysis on either, but both adopt positive Gaussian curvature. The Japanese chainmail network can be constructed out of ropelength-minimizing components in a plane, implying that an ideal configuration need not have the same curvature as a polymer configuration.

### Quadric surface fitting

To perform the quadric surface fitting, we first calculated the center of mass $\mathbf{r}_i^*$ for each ring $i$ and the center of mass $\langle \mathbf{r} \rangle$ for the full chainmail assembly. We then calculated the gyration tensor $G_{ab}$, defined in eqn (6) and found the normalized eigenvectors $\{\hat{\mathbf{e}}_1, \hat{\mathbf{e}}_2, \hat{\mathbf{e}}_3\}$, ordered from largest to smallest eigenvalue. The quadric surface is then given by the set of points $\boldsymbol{\sigma}$, expressed using the Monge representation as

$$\boldsymbol{\sigma}(u_1,u_2) = \langle \mathbf{r} \rangle + u_1\hat{\mathbf{e}}_1 + u_2\hat{\mathbf{e}}_2 + \zeta(u_1,u_2)\hat{\mathbf{e}}_3, \tag{12}$$

where the Monge height function $\zeta(u,v)$ is given by

$$\zeta(u_1, u_2) = \frac{1}{2}u_\mu C_{\mu\nu} u_\nu + B_\mu u_\mu + A_0, \tag{13}$$

where $A_0$ is a scalar, $B_\mu$ are components of a vector $\mathbf{B}$, and $C_{\mu\nu}$ are components of a symmetric matrix $\mathbf{C}$ (where $C_{12} = C_{21}$). The quadric surface is then fit to ring center of mass data by minimizing the residual functional

$$I[A_0, \mathbf{B}, \mathbf{C}] = \frac{1}{M}\sum_{i=1}^{M}\left(r_{i,3}^* - \zeta\left(r_{i,1}^*, r_{j,2}^*\right)\right)^2 \tag{14}$$

over the parameters $A_0$, $\mathbf{B}$, and $\mathbf{C}$. Here, the ring centers $\mathbf{r}_i^*$ have been expressed in the $\{\hat{\mathbf{e}}_1,\hat{\mathbf{e}}_2,\hat{\mathbf{e}}_3\}$ frame as $\mathbf{r}_i^* = r_{i,a}^*\hat{\mathbf{e}}_a$. Finally, the

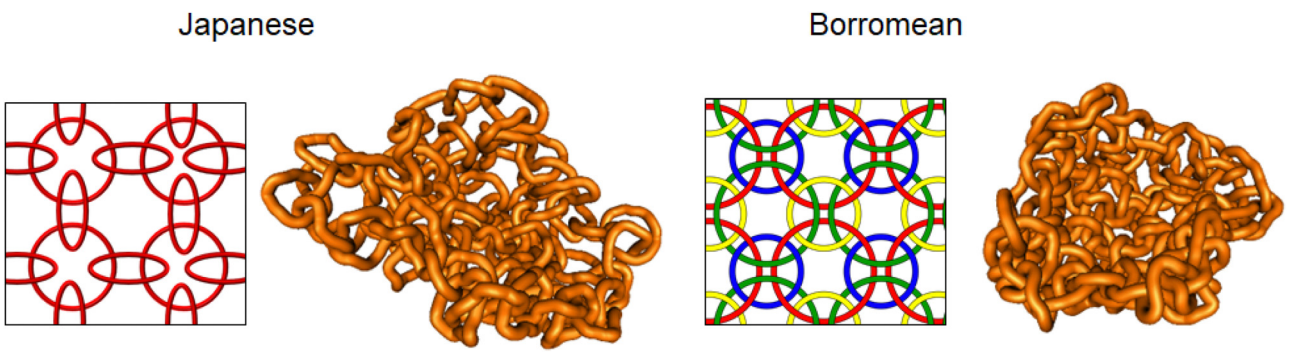


Fig. 11 Design and LAMMPS configurations of Japanese and Borromean chainmail.

Gaussian curvature $K$ is approximated as

$$K \approx \frac{\det \mathbf{C}}{(1+|\mathbf{B}|^2)^2} \tag{15}$$

and the mean curvature $H$ is approximated as

$$H \approx \frac{(1+B_2{}^2)C_{11} - 2B_1B_2C_{12} + (1+B_1{}^2)C_{22}}{2(1+|\mathbf{B}|^2)^{3/2}}. \tag{16}$$

#### Discrete affine connection

The discrete affine connection is a pair of rotation matrices $\mathcal{R}_1$ and $\mathcal{R}_2$. The first of these, $\mathcal{R}_1$, maps the orthonormal frame at ring $(i,\backslash,j)$ to the frame at $(i+1,\backslash,j)$ *via*

$$\begin{pmatrix} \hat{\mathbf{d}}_1^{(i+1,j)} \\ \hat{\mathbf{d}}_2^{(i+1,j)} \\ \hat{\mathbf{N}}^{(i+1,j)} \end{pmatrix} = \begin{pmatrix} \cos\theta_1 & -\sin\theta_1\sin\psi_1 & -\sin\theta_1\cos\psi_1 \\ 0 & \cos\psi_1 & -\sin\psi_1 \\ \sin\theta_1 & \cos\theta_1\sin\psi_1 & \cos\theta_1\cos\psi_1 \end{pmatrix} \begin{pmatrix} \hat{\mathbf{d}}_1^{(i,j)} \\ \hat{\mathbf{d}}_2^{(i,j)} \\ \hat{\mathbf{N}}^{(i,j)} \end{pmatrix}$$
$$= \mathcal{R}_1(\theta_1,\psi_1) \begin{pmatrix} \hat{\mathbf{d}}_1^{(i,j)} \\ \hat{\mathbf{d}}_2^{(i,j)} \\ \hat{\mathbf{N}}^{(i,j)} \end{pmatrix} \tag{17}$$

The second, $\mathcal{R}_2$, maps the orthonormal frame at ring $(i,j)$ to the frame at $(i,j+1)$ *via*

$$\begin{pmatrix} \hat{\mathbf{d}}_1^{(i,j+1)} \\ \hat{\mathbf{d}}_2^{(i,j+1)} \\ \hat{\mathbf{N}}^{(i,j+1)} \end{pmatrix} = \begin{pmatrix} \cos\psi_2 & 0 & \sin\psi_2 \\ \sin\theta_2\sin\psi_2 & \cos\theta_2 & -\sin\theta_2\cos\psi_2 \\ -\cos\theta_2\sin\psi_2 & \sin\theta_2 & \cos\theta_2\cos\psi_2 \end{pmatrix} \begin{pmatrix} \hat{\mathbf{d}}_1^{(i,j)} \\ \hat{\mathbf{d}}_2^{(i,j)} \\ \hat{\mathbf{N}}^{(i,j)} \end{pmatrix}$$
$$= \mathcal{R}_2(\theta_2,\psi_2) \begin{pmatrix} \hat{\mathbf{d}}_1^{(i,j)} \\ \hat{\mathbf{d}}_2^{(i,j)} \\ \hat{\mathbf{N}}^{(i,j)} \end{pmatrix} \tag{18}$$

Taking the small-angle approximation, we $\mathcal{R}_\mu \approx 1 + \mathcal{A}_\mu$, where

$$\mathcal{A}_1 = \begin{pmatrix} 0 & 0 & -\theta_1 \\ 0 & 0 & -\psi_1 \\ \theta_1 & \psi_1 & 0 \end{pmatrix} \qquad \mathcal{A}_2 = \begin{pmatrix} 0 & 0 & \psi_2 \\ 0 & 0 & -\theta_2 \\ -\psi_2 & \theta_2 & 0 \end{pmatrix} \tag{19}$$

which allows us to approximate the resultant rotation matrix $\mathcal{R}_{\text{circ.}}$ around the closed circuit as

$$\mathcal{R}_{\text{circ.}} \approx 1 + [\mathcal{A}_2, \mathcal{A}_1], \tag{20}$$

yielding the result in eqn (9). Here, the commutator $[\mathcal{A}_2,\mathcal{A}_1] \equiv \mathcal{A}_2\mathcal{A}_1 - \mathcal{A}_1\mathcal{A}_2$ measures the holonomy of the discrete connection and represents a discrete calculation of the curvature two-form.[38] Note that the only non-zero component of the commutator is a generator of rotations that leaves the normal fixed, allowing us to immediately relate the magnitude of this term to the Gaussian curvature.

## Acknowledgements

ARK's work is supported by the National Science Foundation, grant number 2122199. We are grateful to Cristian Micheletti, Juan Luengo-Márquez, and Salvatore Assenza for sending us an advanced copy of their manuscript.

## References

1 K. S. Novovselov, A. K. Geim, S. V. Morozov, D. E. Jiang, Y. Zhang and S. V. Dubonos, *et al.*, Electric field effect in atomically thin carbon films, *Science*, 2004, **306**(5696), 666–669.
2 Q. Wu, P. M. Rauscher, X. Lang, R. J. Wojtecki, J. J. De Pablo and M. J. Hore, *et al.*, Poly[*n*]catenanes: Synthesis of molecular interlocked chains, *Science*, 2017, **358**(6369), 1434–1439.
3 X. Liu, J. Tang, Q. Chen and L. Wang, Structurally Switchable Hydrogels with Multifunctions Enabled by Controlled Catenated Junctions, *Macromolecules*, 2024, **57**(1), 174–180.
4 D. P. August, R. A. Dryfe, S. J. Haigh, P. R. Kent, D. A. Leigh and J. F. Lemonnier, *et al.*, Self-assembly of a layered two-dimensional molecularly woven fabric, *Nature*, 2020, **588**(7838), 429–435.
5 F. L. Thorp-Greenwood, A. N. Kulak and M. J. Hardie, An infinite chainmail of M6L6 metallacycles featuring multiple Borromean links, *Nat. Chem.*, 2015, **7**(6), 526–531.
6 T. A. Shapiro and P. T. Englund, The structure and replication of kinetoplast DNA, *Annu. Rev. Microbiol.*, 1995, **49**(1), 117–143.
7 A. R. Klotz, B. W. Soh and P. S. Doyle, Equilibrium structure and deformation response of 2D kinetoplast sheets, *Proc. Natl. Acad. Sci. U. S. A.*, 2020, **117**(1), 121–127.
8 J. M. Polson, E. J. Garcia and A. R. Klotz, Flatness and intrinsic curvature of linked-ring membranes, *Soft Matter*, 2021, **17**(46), 10505–10515.
9 P. He, A. J. Katan, L. Tubiana, C. Dekker and D. Michieletto, Single-molecule structure and topology of kinetoplast dna networks, *Phys. Rev. X*, 2023, **13**(2), 021010.
10 J. Chen, C. A. Rauch, J. H. White, P. T. Englund and N. R. Cozzarelli, The topology of the kinetoplast DNA network, *Cell*, 1995, **80**(1), 61–69.
11 J. Ragotskie, N. Morrison, C. Stackhouse, R. C. Blair and A. R. Klotz, The effect of the kinetoplast edge loop on network percolation, *J. Polym. Sci.*, 2024, **62**(7), 1287–1295.
12 S. Ramakrishnan, Z. Chen, Y. A. G. Fosado, L. Tubiana, W. Vanderlinden, N. J. Savill, *et al.*, *Single-Molecule Morphology*

 

*of Topologically Digested Olympic Networks*, *arXiv*, 2023, preprint, arXiv:231013399, DOI: **10.1103/PRXLife.2.013009**.
13 T. O'Connor, Conference Presentation, Biophysics of Topological Olympic Networks Workshop, University of Edinburgh, 2022.
14 L. Tubiana, F. Ferrari and E. Orlandini, Circular Polycatenanes: Supramolecular Structures with Topologically Tunable Properties, *Phys. Rev. Lett.*, 2022, **129**(22), 227801.
15 M. Dennis and J. Hannay, Geometry of Călugăreanu's theorem, *Proc. R. Soc. A*, 2005, **461**(2062), 3245–3254.
16 J. Luengo-Márquez, S. Assenza and C. Micheletti, Shape and size tunability of sheets of interlocked ring copolymers, *Soft Matter*, 2024, DOI: **10.1039/D4SM00694A**.
17 A. Plummer and D. R. Nelson, Buckling and metastability in membranes with dilation arrays, *Phys. Rev. E*, 2020, **102**(3), 033002.
18 B. W. Soh, A. Khorshid, D. Al Sulaiman and P. S. Doyle, Ionic Effects on the Equilibrium Conformation of Catenated DNA Networks, *Macromolecules*, 2020, **53**(19), 8502–8508.
19 R. G. Scharein and K. S. Booth, Interactive knot theory with KnotPlot, *Multimedia Tools for Communicating Mathematics*, Springer, 2002, pp. 277–290.
20 A. P. Thompson, H. M. Aktulga, R. Berger, D. S. Bolintineanu, W. M. Brown and P. S. Crozier, *et al.*, LAMMPS-a flexible simulation tool for particle-based materials modeling at the atomic, meso, and continuum scales, *Comput. Phys. Commun.*, 2022, **271**, 108171.
21 T. Ashton, J. Cantarella, M. Piatek and E. J. Rawdon, Knot tightening by constrained gradient descent, *Exper. Math.*, 2011, **20**(1), 57–90.
22 M. Meyer, M. Desbrun, P. Schröder and A. H. Barr, Discrete differential-geometry operators for triangulated 2-manifolds, *Visualization and mathematics III*, Springer, 2003, pp. 35–57.
23 Y. Kantor and K. Kremer, Excluded-volume interactions in tethered membranes, *Phys. Rev. E: Stat. Phys., Plasmas, Fluids, Relat. Interdiscip. Top.*, 1993, **48**(4), 2490.
24 D. Kroll and G. Gompper, Floppy tethered networks, *J. Phys. I*, 1993, **3**(5), 1131–1140.
25 H. Popova and A. Milchev, Structure, dynamics, and phase transitions of tethered membranes: A Monte Carlo simulation study, *J. Chem. Phys.*, 2007, **127**(19), 194903.
26 K. I. Mizuochi, H. Nakanishi and T. Sakaue, Dynamical scaling of polymerized membranes, *EPL*, 2014, **107**(3), 38003.
27 M. Gandikota and A. Cacciuto, The crumpling transition of active tethered membranes, *Soft Matter*, 2023, **19**(28), 5328–5335.
28 A. Sardas, M. Moshe and C. Maor, A continuum geometric approach for inverse design of origami structures, *arXiv*, 2024, preprint, arXiv:240507249, DOI: **10.48550/arXiv.2405.07249**.
29 D. V. Kolesnikov and V. A. Osipov, Electronic structure of negatively curved graphene, *JETP Lett.*, 2008, **87**, 419–422.
30 K. Singal, M. S. Dimitriyev, S. E. Gonzalez, A. P. Cachine, S. Quinn and E. A. Matsumoto, Programming mechanics in knitted materials, stitch by stitch, *Nat. Commun.*, 2024, **15**(1), 2622, DOI: **10.1038/s41467-024-46498-z**.
31 A. Košmrlj and D. R. Nelson, Statistical mechanics of thin spherical shells, *Phys. Rev. X*, 2017, **7**(1), 011002.
32 A. Muralidhar, D. R. Tree and K. D. Dorfman, Backfolding of wormlike chains confined in nanochannels, *Macromolecules*, 2014, **47**(23), 8446–8458.
33 J. Cantarella, R. B. Kusner and J. M. Sullivan, On the minimum ropelength of knots and links, *Invent. Math.*, 2002, **150**(2), 257–286.
34 P. M. Chaikin and T. C. Lubensky, *Principles of Condensed Matter Physics*, Cambridge University Press, Cambridge, 1995.
35 M. Kleman and J. Friedel, Disclinations, dislocations, and continuous defects: A reappraisal, *Rev. Mod. Phys.*, 2008, **80**, 61–115.
36 M. F. Hagan and G. M. Grason, Equilibrium mechanisms of self-limiting assembly, *Rev. Mod. Phys.*, 2021, **93**, 025008.
37 S. Meiri and E. Efrati, Cumulative geometric frustration in physical assemblies, *Phys. Rev. E*, 2021, **104**, 054601. Available from: **https://link.aps.org/doi/10.1103/PhysRevE.104.054601**.
38 T. Needham, *Visual Differential Geometry and Forms: A Mathematical Drama in Five Acts*, Princeton University Press, 2021.
39 J. McInerney, B. G. Chen, L. Theran, C. D. Santangelo and D. Z. Rocklin, Hidden symmetries generate rigid folding mechanisms in periodic origami, *Proc. Natl. Acad. Sci. U. S. A.*, 2020, **117**(48), 30252–30259. Available from: **https://www.pnas.org/doi/abs/10.1073/pnas.2005089117**.
40 H. S. Seung and D. R. Nelson, Defects in flexible membranes with crystalline order, *Phys. Rev. A: At., Mol., Opt. Phys.*, 1988, **38**, 1005–1018. Available from: **https://link.aps.org/doi/10.1103/PhysRevA.38.1005**.
41 A. R. Klotz, The tightest knot is not necessarily the smallest, *J. Knot Theory Ramif.*, 2022, **31**(14), 2250102.
42 L. Devroye, *Wikimedia Commons: Borromean Chainmain Tile*, Available from: **https://commons.wikimedia.org/wiki/File:Borromean-chainmail-tile.png**.